Tailoring the $^3F_4$ level lifetime in Tm^{3+}: Y$_3$Al$_5$O$_{12}$ by Eu^{3+} co-doping for signal processing application

Zhonghan Zhang,*[1,2] Anne Louchet-Chauvet,[3] Loïc Morvan,[4] Perrine Berger,[4] Philippe Goldner,[1] and Alban Ferrier*[1,5]

[1] Institut de Recherche de Chimie Paris (IRCP), UniversitéPSL, Chimie ParisTech, CNRS, 75005 Paris, France

[2] Shanghai Institute of Ceramics, Chinese Academy of Sciences, Heshuo Road 585, Jiading, Shanghai, 201899, China

[3] Institut Langevin, CNRS, ESPCI, 1 rue Jussieu, 75005 Paris, France

[4] Thales Research and Technology, 1 Avenue Augustin Fresnel, 91767 Palaiseau, France

[5] Sorbonne Université, Faculté des Sciences et Ingénierie, UFR 933, 75005 Paris, France

Abstract

Tm^{3+}: Y$_3$Al$_5$O$_{12}$ (Tm:YAG) crystal is a promising material for high-resolution spectral analysis of broadband radio-frequency (RF) signals, where the absorption spectrum is modified via spectral hole burning. In Tm:YAG, the efficiency of the spectral tailoring is limited by the long-lived metastable level $^3F_4$, acting as a bottleneck for the optical pumping mechanism. We demonstrate that co-doping Tm:YAG with Eu^{3+} ions can significantly shorten the optical lifetime of $^3F_4$ state, while that of $^3H_4$ is essentially conserved. We show with a model that these modified lifetimes allow faster tailoring of the absorption profile. Because of their low cost and easiness of processing, we use Tm^{3+} and Eu^{3+} co-doped Y$_3$Al$_5$O$_{12}$ ceramics to probe the energy transfer efficiency and find the optimal cation co-doping concentration. Furthermore, we show that Eu^{3+} co-doping increases the inhomogeneous broadening on the Tm^{3+} optical transition, hence the spectral analysis bandwidth. Finally, we confirm these results on a single crystal grown by the Czochralski method.

Key Word: RF signal processing; Eu:Tm:YAG crystal; rare earth spectroscopy; crystal growth

1. Introduction

Rare earth ion-doped single crystals (REIC) are widely used and investigated for various opto-electronics applications, including lighting, laser, sensing [1][2] or more recently quantum information technologies [3][4]. Currently, there is a growing demand for fast, high resolution and broadband RF spectrum analyzers, and REIC are particularly appropriate to build such devices using optical processing based on spectral hole burning (SHB) [5][6]. The basic principle of such application can be described as following: a laser beam is modulated by the radiofrequency (RF) signal to be analyzed and propagated to a REIC crystal cooled down to a few K; The optical sidebands thus created are spectrally analyzed by reading out the absorption profile pattern modified by SHB in the REIC optical transition [7], or by diffracting the modulated beam on spectral gratings obtained by a hole burning sequence performed in advance [8]. The superior performance of the REIC compared to purely electronic spectrum analyzers stems from their broad (>GHz) inhomogeneous absorption profile in the optical

domain, as well as their narrow homogeneous linewidth in the kHz range, which enable both large bandwidth and high spectral resolution [1][5][6].

Several signal processing schemes have been already demonstrated using Tm^{3+} doped $Y_3Al_5O_{12}$ (Tm:YAG) single crystals [5][6]. The most attractive characteristics of this crystal is the 20 GHz inhomogeneous linewidth (Γ_{inh}) of its $^3H_6 \rightarrow {}^3H_4$ optical transition, allowing for wideband spectral analysis of optically-carried RF signals. The homogeneous linewidth Γ_h, which is related to optical coherence time T_2 ($\Gamma_h = \dfrac{1}{\pi T_2}$) and determines the absolute resolution of the system, is relatively narrow, thus providing an ultimate resolution of about 8 kHz [9]. Although this material is currently the most used for RF spectrum analyzers, different approaches have been proposed to improve its performance. For example, several groups proposed to introduce a controlled broadening of Γ_{inh} in order to improve the signal processing bandwidth [10]-[12]. The broadening of the optical transition is induced by an increase of the disorder in the crystal host with a suitable co-doping cation like Sc^{3+} and Lu^{3+} that can increase Γ_{inh} without altering T_2 or the spectral hole's lifetime.

In this paper, we address another limitation of the use of Tm:YAG for spectrum analyzers. For RF signal processing, efficient SHB is obtained by applying a small magnetic field to the sample in order to use Zeeman ground state levels to store populations [13]. In practice, the spectral hole pattern creation involves optical pumping at 793 nm which allows ions to cycle between the ground state $^3H_6$ and excited state $^3H_4$ (Fig. 1). The efficiency of this optical pumping is however limited as most excited ions at $^3H_4$ state will decay to the long lived metastable $^3F_4$ level rather than relax to the ground state. Indeed, the $^3F_4$ optical lifetime is around 10 ms, whereas the $^3H_4$ optical lifetime is only about 500 μs at room temperature. This induces a detrimental bottlenecking because of the stored population in the undesired lower excited states. Moreover, the population stored in the $^3F_4$ level induces a significant erasure of the population grating when the pump laser is switched off, requiring a higher pump duty cycle. A reduction of the optical lifetime in the $^3F_4$ level would reduce the $^3F_4$ state population and is therefore actively desired.
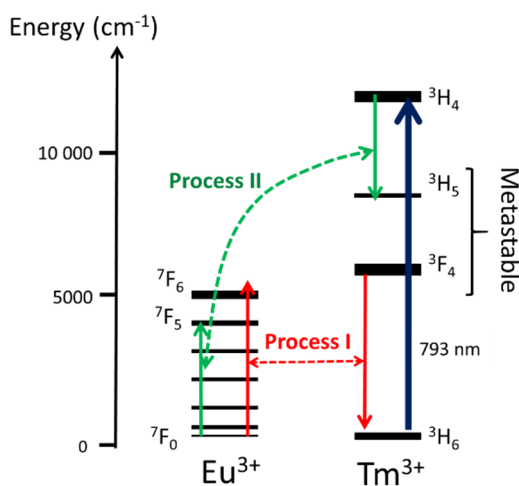
Figure1: Energy level diagram of Tm^{3+} and Eu^{3+} in YAG and energy transfer schemes.

Under the circumstance, we employed the strategy of introducing rare earth co-dopants to selectively reduce the lifetime of the metastable level $^3F_4$. Simultaneously, lifetime of the $^3H_4$

level is expected to be maintained as much as possible, which is necessary to ensure the narrow homogeneous linewidth of the $^3H_4$-$^3H_6$ transition. This lifetime engineering has similarities with the one investigated in the context of 1.54 µm laser emission based on the $^3H_4 \rightarrow ^3F_4$ transition of Tm^{3+}, where the long lifetime of $^3F_4$ level prevents efficient population inversion [14]][[15]. Among the different rare earth ions that could be used as co-dopants, trivalent europium and terbium are the best candidates because they have transitions in close resonance with the $^3F_4$-$^3H_6$ one of Tm^{3+} and can significantly decrease the optical lifetime of $^3F_4$ level. Furthermore, either Eu^{3+} or Tb^{3+} do not absorb around 800 nm, thus would not influence optical pumping process of $^3H_6$-$^3H_4$ transitions of Tm^{3+}. Eu^{3+} is preferred over Tb^{3+} because the latter was found to also significantly decrease the $^3H_4$ lifetime [16]. The structure of energy levels in Eu^{3+} and Tm^{3+} is schemed in Fig. 1. In Eu^{3+} ions the energy gaps between states $^7F_0$ to $^7F_6$ are small enough for efficient non-radiative relaxation, meanwhile the energy of the latter is close to $^3F_4$ in Tm^{3+} ions. Therefore, efficient energy transfer is expected between $^3F_4$ level of Tm^{3+} and $^7F_6$ level of Eu^{3+}(see 'Process I' in *Figure1*). Another unfavorable energy transfer is also expected between the $^7F_0 \rightarrow ^7F_5$ transition of europium and the $^3H_4 \rightarrow ^3H_5$ transition of thulium ('Process II' in *Figure1*), shortening also the $^3H_4$ state lifetime, although such kind of transfer could be could be relatively weaker as the $^7F_0 \rightarrow ^7F_5$ transition of Eu^{3+} is forbidden by the select rule. The two processes are summarized as:

$$(^7F_0, {}^3F_4) \rightarrow (^7F_6, {}^3H_6) \quad \text{Process I}$$
$$(^7F_0, {}^3H_4) \rightarrow (^7F_5, {}^3H_5) \quad \text{Process II}$$
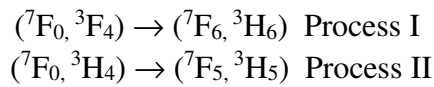
Previous experiments have established that ceramics can be used as an inexpensive and quick way to evaluate compositions prior to undertaking the time and expense involved in single crystal growth. Narrow inhomogeneous and homogeneous linewidth close to the bulk crystal were also demonstrated [12][17]][[18]. Thus, in this paper both ceramics and a single crystal of $Y_3Al_5O_{12}$ co-doped by Eu^{3+} and Tm^{3+} (Eu:Tm:YAG) were investigated. Composition of single crystal was determined according to spectroscopic analysis of ceramic samples of various dopants' concentrations. Synthesis, chemical and structural analysis of both ceramics and single crystal will be presented. Afterwards, spectroscopic characterizations, including absorption spectra, fluorescence decay lifetime as well as inhomogeneous broadening will be discussed in order to assess the potential of such crystals for RF signal processing application.

2. Experiments

YAG exhibits garnet cubic symmetry (Ia-3d) with eight formula units per unit cell. The garnet lattice $A_3B_2C_3O_{12}$ is composed of an oxygen network with 3 different cation sites. In this host, the Y^{3+} cations occupy a dodecahedral (D_2) symmetry site (A) whereas the Al^{3+} cations sit on octahedral (B) and tetrahedral (C) sites. Anti-site defects of the Y_{Al} type could happen in YAG during synthesis process where rare earth cations occupy the Al^{3+} sites. Tm^{3+} and Eu^{3+} substitute the position of Y^{3+} when introduced as dopants.

2.1. Ceramic synthesis and single crystal growth

The ceramic synthesis of YAG has already been discussed in a previous paper [12]. Briefly, ceramics of Tm^{3+} and Eu^{3+} co-doped $Y_3Al_5O_{12}$ were obtained through solid state reaction from

high purity oxide powders (> 99.99%, Alfa Aesar). After room temperature uniaxial pressing, white body pellets were sintered at 1680 ℃ for 20 hours twice with intermediate grinding. Reactions can be summarized as following formula:

$$5Al_2O_3 + 3(1 - x - y)Y_2O_3 + 3xTm_2O_3 + 3yEu_2O_3 \xrightarrow{1680\ ℃} 2Y_{3(1-x-y)}Tm_{3x}Eu_{3y}Al_5O_{12}$$
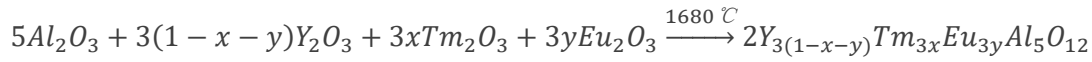
where the Tm^{3+} concentration is $x = 0.5\%$ and the Eu^{3+} concentrations are $y = 0.5\%, 1\%, 2\%, 4\%, 6\%$, respectively. All the concentrations mentioned above are presented in mole percentages.

A single crystal of Eu^{3+} and Tm^{3+} co-doped $Y_3Al_5O_{12}$ (Eu:Tm:YAG) was grown in a homebuilt Czochralski crystal growth apparatus. Based on analysis of the ceramics lifetimes and result of Ref [12], the thulium concentration and europium concentration (see below) in this Eu:Tm:YAG single crystal were determined to be 0.5% and 1%, respectively. This relatively low europium concentration also minimizes possible disturbance of the growth and avoids additional defects. The targeted single crystal composition was therefore $Y_{2.55}(Tm_{0.15}Eu_{0.3})Al_5O_{12}$. A segregation of dopants during the growth is expected since the Tm^{3+}, Eu^{3+} and Y^{3+} radii are different. Since no (Eu,Tm) co-doped YAG growths were reported until now, we used the segregation coefficients determined for Eu or Tm independently. Effective segregation coefficients $k_{Tm} = 0.8$ and $k_{Eu} = 0.6$ were used when preparing raw materials for crystal growth [19]-[21].

An Ir crucible was used to contain melt, while ZrO_2 and Al_2O_3 were used as refractory materials. The growth of the single crystal was performed under flowed nitrogen introduced as a protective atmosphere. The crystal was pulled at a speed of 1 mm/h from the melt using a [111] oriented seed of Tm:YAG. The resulting one-inch diameter single crystal is transparent and colorless with a regular shape (as shown in Figure2(b)). Samples were taken from both the center and the bottom of the crystal boule. They were oriented by Laue X-ray diffraction, cut perpendicular to the [111] direction and optically polished for further measurements.

2.2. **Characterization**

Dopants' concentrations in the single crystal were measured by electron probe micro-analysis (EPMA) using an SX Five CAMECA analyzer. The purity of the ceramics as well as single crystal samples was also determined through Powder X-ray diffraction measurements (PXRD) performed on a Panalytical XPert Pro diffractometer with an incident beam Ge monochromator. The patterns were recorded over 3 hours or 12 hours up to 130° with 0.013° steps. Rietveld analyses were carried out with the FullProf software to determine lattice parameters [22].

Room temperature absorption spectra of Eu:Tm:YAG single crystal were collected from UV to IR region. Spectra in the UV, visible and near-IR regions were measured by a Cary 6000i spectrophotometer using a spectral bandwidth (SBW) setting of 0.1 nm, meanwhile measurements in the IR region were performed by a Cary 5000 spectrophotometer using SBW setting of 0.5 nm within range of 1500 nm to 2200 nm and SBW setting of 2 nm within range of 2200 nm to 2850 nm. Spectra of samples fabricated at the center and bottom of the Eu:Tm:YAG crystal boule were collected for comparison. A sample of 0.4% Tm^{3+} doped $Y_3Al_5O_{12}$ single crystal, which was grown previously in our group, was also measured as a

reference [12]. Absorption coefficients of different dopants were calculated and compared to determine the concentrations of dopants, as a supplementary to EPMA measurement.

Fluorescence decay measurements of the $^3H_4$ and $^3F_4$ states of Tm^{3+} ions in ceramic and single crystal samples of Eu:Tm:YAG were performed to determine their optical lifetime, both at room temperature and at 15 K using a Janis closed-cycle cryostat. For the measurement of the $^3H_4$ decay, an OPO laser (EKSPLA) was tuned at 785 nm to pump Tm^{3+} from ground state $^3H_6$ to $^3H_4$ level. The fluorescence signal was collected from the perpendicular direction by a photomultiplier after selected at 835 nm by a monochromator, corresponding to the $^3H_6 \rightarrow {}^3H_4$ transition. For the measurements of the $^3F_4$ decay, the OPO pump source was tuned at 1198 nm to excite Tm^{3+} to $^3F_5$ state, and all the pumped Tm^{3+} ions will afterwards relax to the $^3F_4$ state through phonon relaxation. As the intensity of the $^3F_4 \rightarrow {}^3H_6$ fluorescence around 2 μm is very weak, it was directly collected using a liquid-N_2-cooled InSb detector (Cincinnati Electronics model SDD-32E0-S1, 100 ns rising time) perpendicular to pump laser after a long-pass filter (cut-on wavelength at 1860 nm).

The inhomogeneous linewidth of the $^3H_6$ to $^3H_4$ transition in both ceramics and single crystal was measured at 10 K using a closed-cycle cryostat. For opaque ceramics we performed fluorescence excitation experiments by monitoring the $^3H_4 \rightarrow {}^3F_4$ 1.5 μm transition while scanning the excitation around 793 nm provided by a Coherent 829 Ti:Sapphire laser (4 GHz linewidth). The pump laser power sent to the sample is adjusted to be around 3.2 mW in order to prevent radiative thermal heating. The 1.5 μm fluorescence was collected through a side window of the cryostat, filtered by a 35 nm-wide interferometric bandpass filter centered at 1543 nm, and focused on an amplified InGaAs photodiode (Thorlabs PDA20CS-EC). For the measurement of single crystal, we directly performed transmission experiments using a silicon amplified photodiode (Thorlabs PDA36A-EC) as a detector.

3. Results and discussion

3.1. Powder X-ray Diffraction (PXRD)
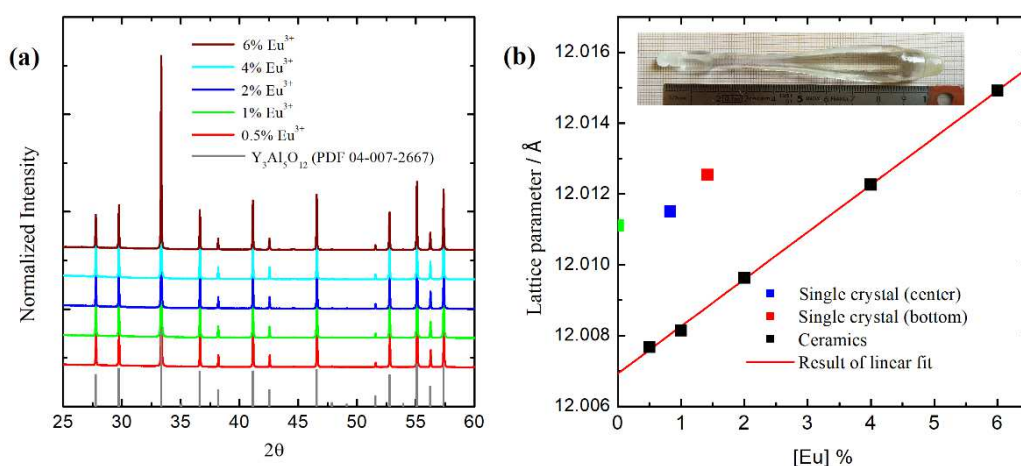
Figure2: (a) The PXRD patterns of Eu:Tm:YAG ceramics. Reference pattern of cubic YAG (PDF:04-007-2667 [25]) is shown at the bottom for comparison. (b) Crystal lattice parameters

obtained by Rietveld analysis (squares) and linear fit (line). Inset: Photo of Eu:Tm:YAG single crystal grown by Czochralski technique.

Fig. 2(a) summarizes the result of PXRD measurements in ceramics. The diffraction pattern is fully indexed with the garnet phase, indicating the high purity of the samples. The effect of Eu^{3+} substitution on the cell parameter is reported on Fig. 2(b). Crystal lattice parameters increase linearly with Eu^{3+} concentration, and a fit to the data gives $a = 12.00693 + 0.00133 * C_{Eu}$, where C_{Eu} is the concentration of Eu^{3+} in unit of percentage. That linear behavior agrees with Vegard's rule and indicates the existence of a solid solution between Eu^{3+} and Y^{3+} cations. It is moreover consistent with the ionic radius mismatch between Eu^{3+} (1.07 Å) and Y^{3+} ions (1.019 Å) [22][24]. Indeed, the radius mismatch is about 0.051 Å and an increase in the cell parameter is expected.

The lattice parameters of two samples fabricated at two positions in the single crystal is also plotted in Fig. 2(b). The Eu^{3+} concentrations in them, i.e., their positions at horizontal axis in the figure, is obtained by the EMPA measurement. The lattice parameter is around 12.0115 Å at the center part of the boule and increases to 12.0125 Å at the bottom part. The increase of the cell parameter during the growth indicates an increase in Eu^{3+} concentration as expected for an effective segregation coefficient of $k_{eff} < 1$. These two values are nevertheless close to the value reported for Tm:YAG single crystal where a lattice parameter of 12.0111 Å is observed [8].

The comparison between the cell parameter of the ceramics and single crystals at the same Eu^{3+} concentration shows a relatively large discrepancy. The larger cell parameter observed in single crystals is attributed to the presence of yttrium, thulium or europium on octahedral aluminum anti-sites (Y_{Al}, Tm_{Al} or Eu_{Al}). Indeed, several studies report that a larger amount of anti-site defects appears when the processing temperature increases [26]-[28]. In our case, the Czochralski growth temperature is estimated at about 2100°C by optical pyrometry and is considerably higher than the temperature used to synthesize ceramics.

3.2. **Single crystal absorption spectra**
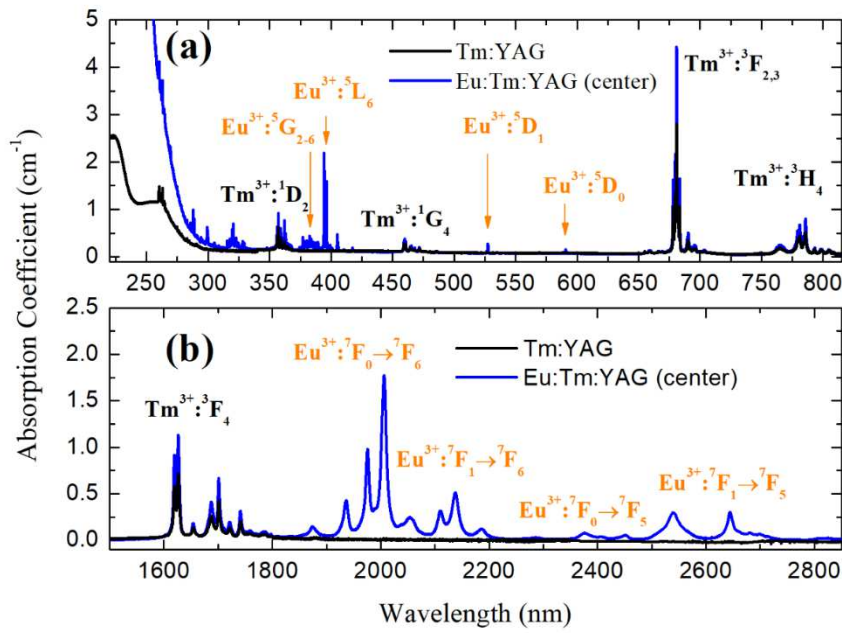
Figure3:Blue line: Absorption spectra of Eu:Tm:YAG single crystal (center part) at room temperature in UV-visible (a) and IR region (b). Transitions of Tm^{3+} and Eu^{3+} are labeled in black and orange, respectively. Black line: The spectra of Tm:YAG single crystal are also shown for comparison.

Absorption spectra of the Eu:Tm:YAG single crystal in the UV-Visible (250 nm to 820 nm) and IR (1500 nm to 2850 nm) regions at room temperature are shown inFig.3. Absorption spectra of a previous grown Tm:YAG sample, whose Tm^{3+} concentration was determined to be 0.4% by EPMA measurement, are also shown for comparison. Saturated absorption is observed with a longer cut-off wavelength at UV range in Eu:Tm:YAG crystal compared to Tm:YAG sample, due to charge transfer band of Eu^{3+} ions. Rare earth ions' absorption peaks are labeled with the corresponding excited states of the transitions originating from the $^7F_{0,1}$ and $^3H_6$ ground states of Eu^{3+} and Tm^{3+} respectively. The Eu^{3+} absorption bands are divided in two categories, *i.e.,* those located at a wavelength shorter than 650 nm, corresponding to excited states with energy higher than the $^5D_0$ state, and those located in the IR region with wavelength longer than 1.8 μm, corresponding to the ^7F_J states. In particular, by comparing the absorption spectra of Eu:Tm:YAG and Tm:YAG crystals, we confirmed that the absorption around 793 nm, which is the wavelength of Tm^{3+}: $^3H_6 \rightarrow {}^3H_4$ line used in spectral analyzers, is only contributed by the Tm^{3+} ions in the Eu:Tm:YAG sample.

By comparing the absorption spectra of samples fabricated from the center and bottom parts of the boule, segregation of both Tm^{3+} and Eu^{3+} is clearly evidenced. Room temperature absorption spectra of the two Eu:Tm:YAG samples around 680 and 395 nm, which correspond respectively to Tm^{3+}: $^3H_4 \rightarrow {}^3F_{2,3}$ and Eu^{3+}: $^7F_{0,1} \rightarrow {}^5L_6$ transitions, are plotted in Figure4. Spectrum of the 0.4% Tm:YAG single crystal sample around 680 nm is also shown for comparison. It can be indicated that Tm^{3+} concentration in the center part is slightly higher than that in the bottom part, whereas Eu^{3+} concentration behaves in the opposite way: it is much higher in the bottom part than in the center area.
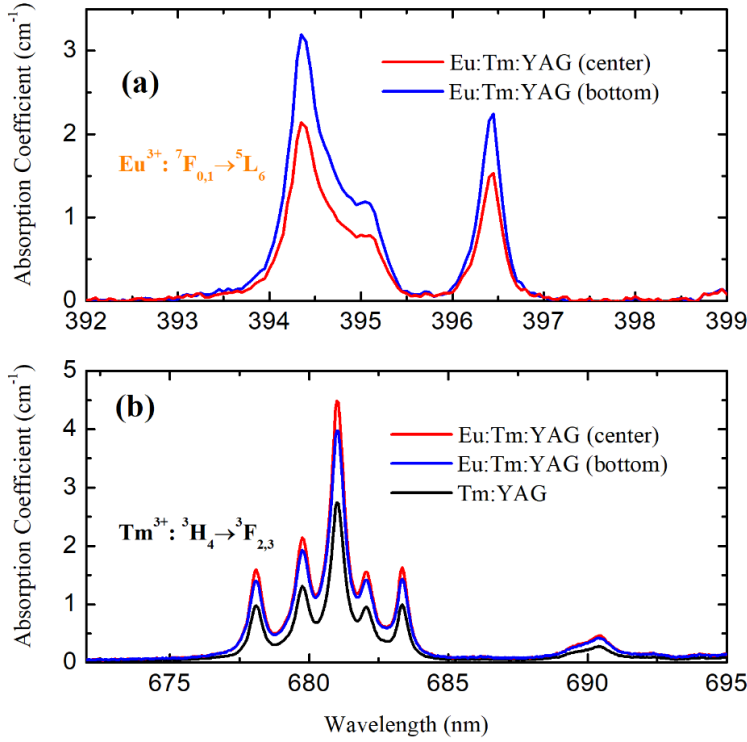
Figure4: Room temperature absorption spectra of Tm^{3+}:$^3H_6 \rightarrow ^3F_{2,3}$ (a) and Eu^{3+}: $^7F_0 \rightarrow 5L_6$ (b) transitions at the center and bottom of Eu:Tm:YAG boule and in a sample of 0.4% Tm:YAG.

Absorption coefficients at the peak wavelengths, which is 681 nm for the Tm^{3+}:$^3H_6 \rightarrow ^3F_{2,3}$ transition and 394.35 nm for the Eu^{3+}:$^7F_0 \rightarrow ^5L_6$ transition respectively, were obtained from absorption spectra to estimate the doping concentrations. Tm^{3+} concentrations in the Eu:Tm:YAG crystal samples were then calculated by comparing their absorption coefficients with those obtained in the reference Tm:YAG sample, whose Tm^{3+} concentration was already determined to be 0.4% by EPMA measurement [12], while the concentrations of Eu^{3+} in Eu:Tm:YAG samples were calculated by comparing to the absorption cross-sections given in Ref. [29]. Concentrations of rare earth dopants calculated from absorption spectra are shown in Table 1, together with results of EPMA measurement for comparison.

Table1: Concentrations of rare earth dopants obtained by analyzing these spectra in Fig. 4 and by EPMA measurement.

	Tm:YAG	Eu:Tm:YAG (center)	Eu:Tm:YAG (bottom)
α of Tm:$^3F_{2,3}$ absorption (cm^{-1})	2.745	3.979	4.486
C_{Tm} (%) obtained by α	-	0.62	0.66
C_{Tm} (%) from EPMA	0.4	0.74	0.61
α of Eu:$^5L_6$ absorption (cm^{-1})	-	2.14	3.19
C_{Eu} (%) obtained by α	-	1.025	1.53
C_{Eu} (%) from EPMA	0	0.8	1.42

It can be indicated that concentrations of rare earth dopants obtained from absorption coefficients calculations are relatively close to that obtained by EPMA measurement, therefore the results of EPMA measurement are applied in this paper to label dopants' concentrations in

crystal samples. As mentioned in section 3.1, we used segregation coefficients $k_{Eu} = 0.6$ and $k_{Tm} = 0.8$ when we prepared the growth of the single crystal. The actual concentration of dopants in the melt was therefore 0.625% for Tm^{3+} ion and 1.67% for Eu^{3+} ion. The results given in Table1 indicate that $k_{Eu} = 0.5 \sim 0.6$ was a reasonable value meanwhile k_{Tm} was slightly larger than 1 instead of 0.8. We attribute this discrepancy to the presence of Eu^{3+} as a co-dopant: since $R_{Eu} > R_Y$, Eu doping enlarges the YAG lattice, which makes it easier for Tm^{3+} to occupy Y^{3+} sites. This effect has already been observed in garnets for other co-doping like Sc^{3+} [12].

3.3. Fluorescence decay times of the $^3H_4$ and $^3F_4$ states of Tm^{3+} in Eu:Tm:YAG

Figure5 shows the fluorescence decay of Tm^{3+} states $^3H_4$ and $^3F_4$ for various Eu^{3+} contents in the ceramics and single crystal at 15 K. Intensity of all these spectra at t = 0 was normalized to have a better comparison. Note that for the $^3H_4$ state decay of Eu:Tm:YAG single crystal, only the result of the sample from center part of the boule is plotted in Fig 5(a) as the decay curve of the other sample from the bottom part is very similar. It can be indicated that decay times of both states decrease when concentration of Eu^{3+} increases, meanwhile the influence of Eu^{3+} dopant is much more obvious for the $^3F_4$ state. A similar result was obtained for fluorescence decay measurements at room temperature. Averaged lifetimes T_1 were obtained by integrating the intensity-time product over time:

$$T_1 = \frac{\int_0^\infty I(t)t\, dt}{\int_0^\infty I(t) dt} . \qquad (1)$$

The results for the $^3H_4$ and $^3F_4$ levels are summarized inTable 2. A decrease of both $^3H_4$ and $^3F_4$ lifetimes is observed when the Eu^{3+} content increases, in agreement with our expectations (see Figure1), together with an increasing non-exponential behavior. In addition, the magnitude of T_1 reduction is larger for $^3F_4$ state than for $^3H_4$. We use the Burshtein model [30][29] to fit the $^3F_4$ and $^3H_4$ decays, using the expression:

$$I = I_0 e^{\left(-\frac{t}{\tau_D} - \gamma\sqrt{t}\right)} \qquad (2)$$

where τ_D and γ represent the level lifetime of Tm^{3+} in Tm:YAG and energy transfer parameter, respectively.
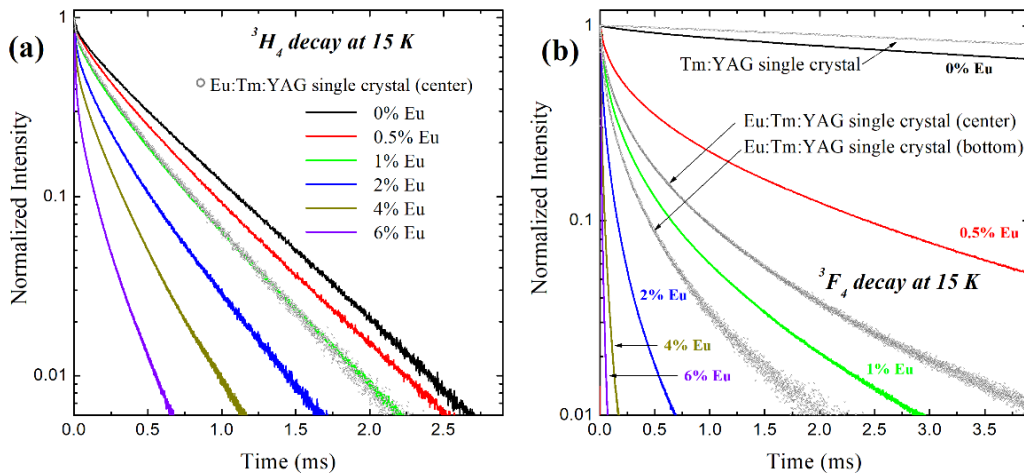
Figure5: Decay curves of $^3H_4$ state (a) and $^3F_4$ state (b) of Tm^{3+} in Eu:Tm:YAG ceramics and single crystals at 15 K. Results of ceramics are plotted by colored lines and labeled by their Eu^{3+} concentrations, while single crystal samples are plotted by gray dots and labeled independently.

We note that for both samples of Eu:Tm:YAG single crystal, the optical lifetime T_1 of $^3F_4$ state is still longer than that of the $^3H_4$ state, but the difference is only about a factor of 2; meanwhile, T_1 of $^3F_4$ state in the center part of the boule is obviously longer than in the bottom part. This supplement the result of the analysis of dopants' concentrations, *i.e.,* Eu^{3+} concentration is higher at the bottom of the boule, as discussed in section 3.2.

Table2: Averaged decay lifetimes T_1 of $^3H_4$ and $^3F_4$ states of Tm^{3+} at both room temperature (295 K) and 15 K in ceramics and single crystal samples.

	Concentrations of dopants	Room Temperature		15 K	
		$^3H_4$ (ms)	$^3F_4$ (ms)	$^3H_4$ (ms)	$^3F_4$ (ms)
YAG Ceramics	0.5%Tm^{3+}	0.47	9.8	0.54	14.28
	0.5%Eu^{3+}, 0.5%Tm^{3+}	0.31	1.9	0.51	2.82
	1%Eu^{3+}, 0.5%Tm^{3+}	0.28	0.72	0.44	0.82
	2%Eu^{3+}, 0.5%Tm^{3+}	0.25	0.23	0.34	0.21
	4%Eu^{3+}, 0.5%Tm^{3+}	0.14	0.05	0.23	0.04
	6%Eu^{3+}, 0.5%Tm^{3+}	0.08	0.02	0.13	0.02
YAG Crystals	0.4%Tm^{3+}	0.51	11.4	0.57	15.38
	0.8%Eu^{3+}, 0.74%Tm^{3+} (Center)	0.38	0.87	0.43	1.06
	1.42%Eu^{3+}, 0.61%Tm^{3+} (Bottom)	0.28	0.5	0.39	0.51

The variation of the transfer parameter γ derived from Eq. (2) with respect to the Eu^{3+} concentration and the temperature is presented inFig.6. Transfer parameters γ show a linear increase with Eu^{3+} content, meanwhile $\gamma\,(^3F_4)$ is one order of magnitude larger than $\gamma\,(^3H_4)$. We attribute this large discrepancy to the difference in the oscillator strength of the Eu^{3+} absorption band. Indeed, the Eu^{3+}: $^7F_0 \rightarrow {}^7F_5$ transition that resonate with Tm^{3+}: $^3H_4 \rightarrow {}^3H_6$ transition and shorten the T_1 of Tm: $^3H_4$ state is electric dipole forbidden and is much weaker than the Eu^{3+}: $^7F_0 \rightarrow {}^7F_6$ and $^7F_1 \rightarrow {}^7F_5$ transitions, which can be also indicated according to their absorption strengths shown in Fig.3(b). Therefore, the influence of the Eu^{3+} co-dopant is more efficient on process I inFigure 1.
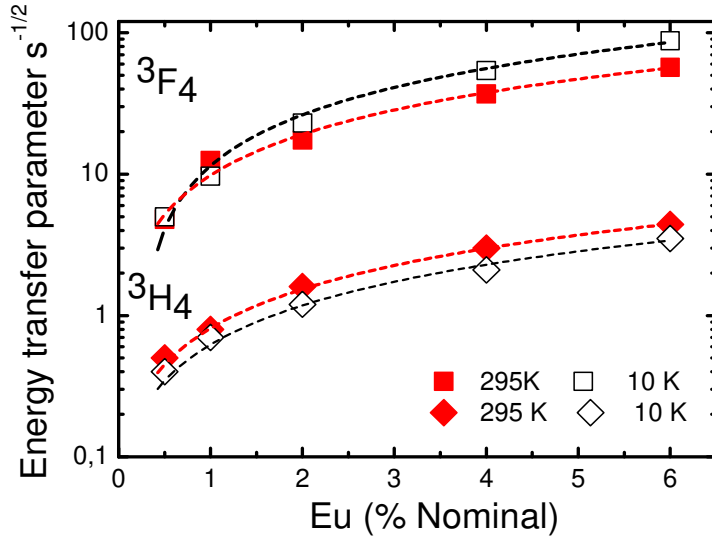
Figure6: Variation of the energy transfer parameter γ(s⁻¹ᐟ²) for the ³H₄ and ³F₄ transition at 15 K (open symbols) and 295 K (solid symbols). The dotted line represents the linear fits of the experimental points. Note that we used semi-log scale in vertical axis.

According to the Eu^{3+} energy level structure [22], processes I and II are both exothermic since the energy gap between the Eu^{3+} levels are smaller than the gap between the Tm^{3+} levels. The energy transfers are therefore assisted by phonon emission. The slight modification of the energy transfer parameter with respect to temperature is attributed on one hand to the reduction of the phonon transition processes, and on the other hand to a change of the population distribution, that lead to small change in the overlap integral. The two processes, although become weaker as temperature decreases, are still efficient even at cryogenic temperature, which is favorable for application as spectral analyzer, as low temperature is necessary in order to decrease Γ_h and reduced the relaxation process in order to have narrow hole and long Zeeman lifetime.

3.4. Rate equation model

We use a rate equation approach to theoretically investigate the effect of energy transfer on the Tm^{3+} optical pumping mechanism. In our model, N_1 and N_2 are the populations of the two hyperfine states of the lowest ³H₆ crystal field level, meanwhile N_3 is the population of the ³F₄ level. ³H₅ is assumed to quickly relax to ³F₄ by non-radiative decay and its population is neglected. N_4 is the population of the pumping level ³H₄. This four-level system is sufficient for describing the whole system [1][31]. The rate equations for the system are:

$$\frac{dN_1}{dt} = \frac{N_4\beta_{41}}{\tau_4} + \frac{N_3\beta_{31}}{\tau_3} + \frac{N_2}{2\tau_Z} - \frac{N_1}{2\tau_Z}$$

$$\frac{dN_2}{dt} = \frac{N_4\beta_{42}}{\tau_4} + \frac{N_3\beta_{32}}{\tau_3} - \frac{N_2}{2\tau_Z} + \frac{N_1}{2\tau_Z} - R_2N_2$$

$$\frac{dN_3}{dt} = \frac{N_4\beta_{43}}{\tau_4} - \frac{N_3}{\tau_3}$$

$$\frac{dN_4}{dt} = - \frac{N_4}{\tau_4} + R_2N_2 \tag{3}$$

where τ_i and β_{ij} are the lifetime of level i and the branching parameter between levels i and j respectively. τ_Z is the Zeeman lifetime and R_2 is the pumping rate.

We are interested in populations in levels 1 and 2 which are used for storing the population in the hole burning process. In particular, we focus on the N_1/N_2 ratio which gives the contrast of the spectral grating for small absorptions. Using the steady-state condition we can derive the ratio for the two hyperfine levels as:

$$\frac{N_1}{N_2} = \frac{(\beta_{31}\beta_{43}+\beta_{41})\times(2\tau_Z R_2+1)+\beta_{32}\beta_{43}+\beta_{42}}{(\beta_{31}\beta_{43}+\beta_{41})+(\beta_{32}\beta_{43}+\beta_{42})} \tag{4}$$

We note that the steady-state ratio N_1/N_2 depends neither on τ_3 nor on τ_4, *i.e.,* on the population stored in the excited states, but only on the branching ratios, pump rate and Zeeman lifetime. Instead, lifetimes τ_3 and τ_4 play a role before the steady-state is reached, as demonstrated by the numerical calculation using Runge-Kutta method (matlab ODE45 solver) inFig.7. Parameters of $\beta_{41} = 0$, $\beta_{42} = 0.3$, $\beta_{43} = 0.7$, $\beta_{32} = 0.67$, $\beta_{31} = 0.33$, $\tau_Z = 230$ ms and $R_2 = 50000$ s^{-1} are used in the simulation. The necessary time to reach the steady-state is shorter for the co-doped sample, while the population ratio is similar. Therefore, the pumping duration could be in principle significantly reduced.
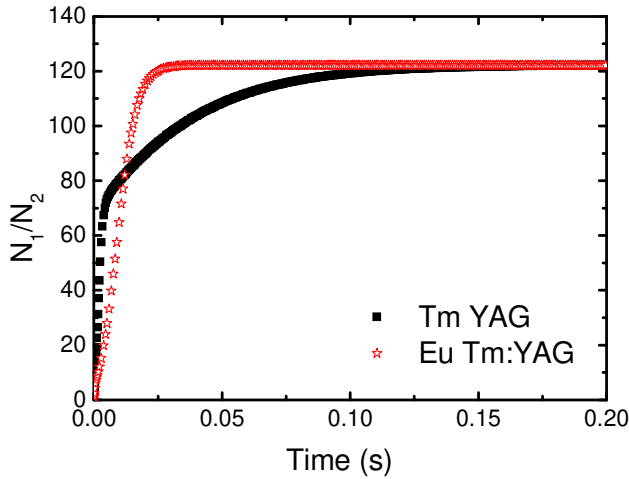
Figure7: Variation of the hyperfine population ratio (N_1/N_2) with time simulated by numerical calculation. Squares and stars represent the simulation for Tm:YAG and Tm,Eu:YAG respectively.

After the pump is turned off or tuned to burn a grating at new frequency, the populations stored in levels 3 and 4 will relax to levels 1 and 2 and modify N_1/N_2 ratio. In the following calculations and simulations, we assume that the pump is turned off at t_0 after steady state is reached and that after a delay δt levels 3 and 4 have fully relaxed, while $\delta t \ll \tau_Z$. Moreover, to obtain analytical expressions, and the pumping rate is taken as very high so that we have $N_1 \approx 1$ and $N_2 \approx 0$. Then the population ratio at $t_0 + \delta t$ is:

$$\frac{N_1}{N_2} = \frac{(\beta_{41}\beta_{43}+\beta_{31})\times(2\tau_Z\beta_{43})}{\beta_{42}\tau_4+(\tau_3+\tau_4)\times\beta_{32}\beta_{43}+(\beta_{41}\beta_{43}+\beta_{31})\times\beta_{43}\delta t} \tag{5}$$

It increases linearly with increasing τ_Z, reflecting the pumping stage, but decreases with increasing τ_3 and τ_4. This is explained by the relaxation from these levels to level 2, as shown by the factors $\beta_{42}\tau_4$ and $\beta_{43}\beta_{32}(\tau_3 + \tau_4)$ in the denominator. The last term on the denominator

is due to the relaxation between the Zeeman levels. Figure8 shows calculated N_1/N_2 ratios solving numerically Eq. 4 and using Eq. 5, as a function of τ_Z for Tm:YAG ($\tau_3 = 10$ ms, $\tau_4 = 0.5$ ms, and $\delta t = 40$ ms) and Eu:Tm:YAG ($\tau_3 = 1$ ms, $\tau_4 = 0.5$ ms, and $\delta t = 40$ ms). When $\tau_Z = 2$ s [31], N_1/N_2 is 39% higher in Eu,Tm:YAG than in Tm:YAG. We note that further increase of Eu co-doping, i.e., decrease of both τ_3 and τ_4 would be beneficial until τ_4 starts to impact the 1-4 and 2-4 transition homogeneous linewidths.
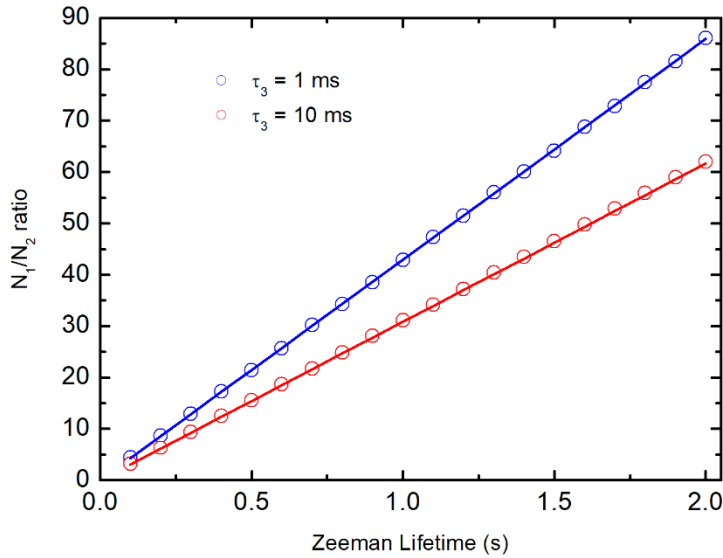
Figure8: Zeeman population lifetime ratio as function of τ_Z after relaxation of the excited states. Circles: numerical simulation. Lines: theoretical calculation from equation 5.

3.5. **Inhomogeneous broadening measurement**

Due to the random substitution between Y^{3+} and Eu^{3+} cations, which have different ionic radii, co-doping with europium induces strain in the lattice and increases the inhomogeneous linewidth on the Tm^{3+} optical transition. The inhomogeneous broadened absorption profiles of $^3H_6 \rightarrow ^3H_4$ in our ceramics and single crystals are presented in Figure9. A significant broadening occurs with no detectable central frequency shift. Furthermore, the absorption band has a Lorentzian line-shape, as expected when the broadening is induced by low concentration point defects such as Eu^{3+} [32].
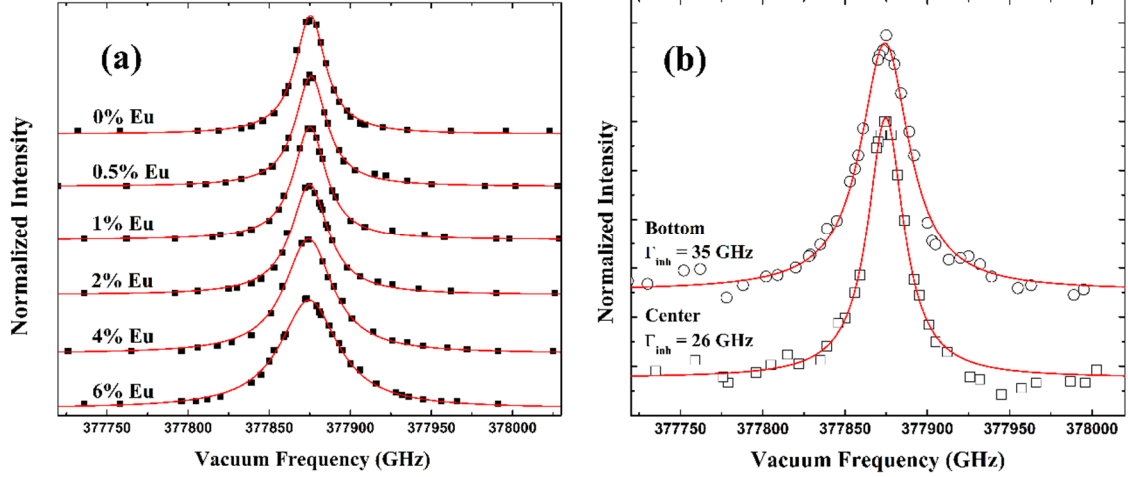
Figure9: (a) Excitation spectra of $Tm^{3+}:^3H_6 \rightarrow ^3H_4$ transition of the ceramics at 10 K by probing the 1.54 μm transition. Tm^{3+} concentration in all these samples is 0.5%. (b) Inhomogeneous absorption line of the $Tm^{3+}:^3H_6 \rightarrow ^3F_4$ transition in Eu:Tm:YAG single crystal samples at 10 K.

The full width at half maximum (FWHM) values of the fitted Lorentzian functions for all these spectra in Fig. 9 are plotted in Figure10. Similar with the result described recently for Sc^{3+} co-doping [12] in Tm:YAG, a linear increase of the broadening is also observed when Eu^{3+} concentration is higher than 1%. However, the 3.6 GHz/Eu% broadening factor in Eu:Tm:YAG is much lower as compared to 24 GHz/Sc% in Sc^{3+} doped Tm:YAG sample. We attribute this difference to the different volume of substitute polyhedral. Indeed, the Sc^{3+} ions substitute mainly in the octahedral site of the garnet structure whereas the Eu ions substitute to Y^{3+} in the larger dodecahedral site. The relative variation in radius is about 39% and 5% for the Sc^{3+} and Eu^{3+} respectively [24]. Therefore, the distortion introduced by Sc^{3+} dopant should be much larger.

A similar broadening is observed in the single crystal of Tm:Eu:YAG. The inhomogeneous broadening of the sample cut from the center part of the boule is around 26 GHz, slightly larger than the inhomogeneous broadening of the Eu:Tm:YAG ceramic sample with 1% Eu^{3+} concentration. This small deviation is also observed in Ref [12] and is due to an increase of yttrium anti-site defects in the single crystal in comparison to the ceramics, which is also in consistent with lattice parameter analysis (see Figure2). On the other hand, the small increase of Eu^{3+} concentration between the two slices of the single crystal cannot explain the large broadening (35 GHz) observed for the bottom part. It is certainly due to additional defects appearing during the end of the growth. Indeed, the change of the dopant concentration in the melt during the growth can lead to modification of the growth interface or superficial tension that induces additional defect formation, especially at the end of the crystal growth. [33] This growth perturbation is confirmed by studying different crystal slice samples using a cross polarization transmission setup. As shown in the inset of Figure10, an unusually large inhomogeneous, strain-induced birefringence throughout the bottom sample is observed whereas the homogeneity of birefringence in the center sample is much better. Tiny inclusions can be also identified at the edge of the bottom sample, which is due to impurity introduced at the end stage of the growth process. As the inhomogeneous linewidth appears to be very

sensitive to material quality and to the doping concentration, the unusual large broadening observed in the bottom sample is probably due to its more compressed defects.
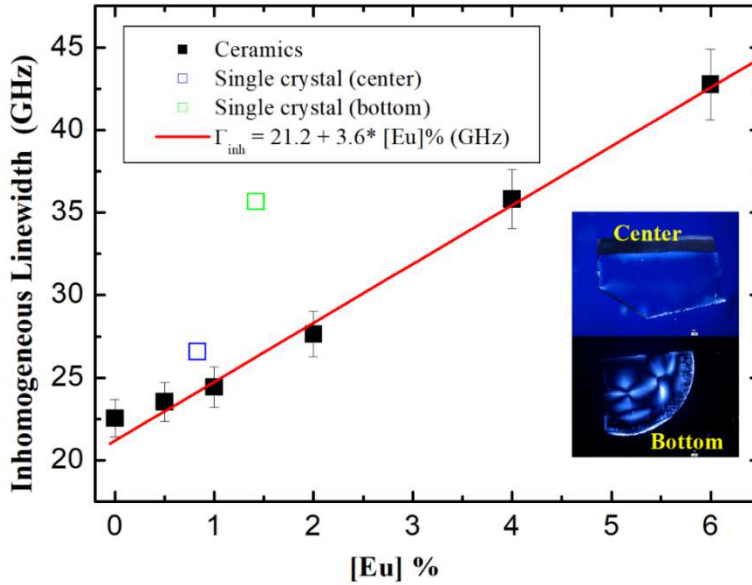
Figure10: Variation of the inhomogeneous linewidth of the $^3H_6 \rightarrow {}^3H_4$ transition at 10 K in Eu:Tm:YAG ceramics for different Eu^{3+} concentrations (solid squares) as well as in two slices of single crystals (Open squares). Red line is the linear fit for result of ceramics within [Eu]% range from 0.5% to 6%. The inset shows the photos of these two single crystal slices under cross polarization microscope.

4. Conclusion

In this paper, ceramic samples of YAG doped with 0.5% Tm^{3+} and 0.5%~6% Eu^{3+} were synthesized, and a single crystal of Eu:Tm:YAG was grown using the Czochralski method. X-ray diffraction and electron probe characterization showed an increase in the Tm^{3+} segregation coefficient in the co-doped sample whereas the segregation coefficient of europium does not seem to be modified by the presence of Tm^{3+}. In addition, a large difference in Eu^{3+} concentration was observed at different positions in the crystal boule.

Fluorescence decay measurements indicated that the optical lifetimes T_1 of the $^3F_4$ state in Tm^{3+} is considerably decreased due to strong energy transfers between Tm^{3+} and Eu^{3+}. A weaker energy transfer shortens the $^3H_4$ level lifetime to a lesser extent. Rate equation simulations showed that more efficient optical pumping should be possible with a faster duty cycle in the co-doped crystal, which is of particular interest for RF signal processing applications. Moreover, the inhomogeneous linewidth of Eu:Tm:YAG is broadened due to Eu^{3+} dopant, which is also advantageous in RF signal processing applications where the processing bandwidth is given by the inhomogeneous broadening of the optical transition.

In conclusion, introducing Eu^{3+} into Tm:YAG crystals seems to be an efficient approach to increase both programming speed and detection bandwidth for RF signal processing applications. Further characterizations are in progress, in particularly concerning coherence

properties and spin population lifetimes, in order to learn the validity of this material for such applications.

References

[1] B. Jacquier and G. Liu, Spectroscopic properties of rare earths in optical materials, Vol. 83, ISBN 3-540-23886-7, Springer-Verlag Berlin Heidelberg (2005).

[2] W. M. Yen, S. Shionoya and H. Yamamoto, Phosphor Handbook, 2nd edition, ISBN 9780849335648 CRC Press (2006).

[3] P. Goldner, A. Ferrier and O. Guillot-Noël, Rare earth-doped crystals for quantum information processing, in: J.-C. Bünzli, V. K. Pecharsky (Eds.), Handbook on the Physics and Chemistry of Rare Earths, Elsevier, Amsterdam, 1–78, (2015).

[4] W. Tittel, M. Afzelius, T. Chanelière, R. L. Cone, S. Kröll, S. A. Moiseev and M. J. Sellars, Laser & Photon. Rev. 4, 244–267, (2010).

[5] C. W. Thiel, T. Böttger and R. L. Cone, J. Lumin. 131, 353, (2011).

[6] P. Berger, Y. Attal, M. Schwarz, S. Molin, A. Louchet-Chauvet, T. Chanelière, J.-L. Le Gouët, D. Dolfi and L. Morvan, J. Lightwave Tech. 99, (2016).

[7] F. Schlottau, M. Colice, K. H. Wagner and W. R. Babbitt, Opt. Lett. 30, 3003 (2005).

[8] L. Ménager, I. Lorgeré, J.-L. Le Gouët, D. Dolfi and J.-P. Huignard, Opt. Lett. 26, 1245 (2001).

[9] R. M. Macfarlane, Opt. Lett. 18, 1958 (1993).

[10] C. W. Thiel, N. Sinclair, W. Tittel and R. L. Cone Phys. Rev. B 90, 214301, (2014).

[11] K. D. Merkel, C. R. Stiffler, A. Woidtke, A. Traxinger, R. W. Equall etc., US patent No.: US 8,829,471 B1, (2014).

[12] A. Ferrier, S. Ilas, P. Goldner and A. Louchet-Chauvet. J. Lumin. 194, 116-122, (2018).

[13] H. Linget, T. Chaneliere, J.-L. Le Gouët, P. Berger, L. Morvan and A. Louchet-Chauvet, Phys. Rev. A 91, 023804, (2015).

[14] A. Braud, S. Girard, J. L. Doualan and R. Moncorgé, IEEE J. Quantum. Electron. 34, 2246-2255, (1998) .

[15] R. Lisiecki, W. Ryba-Romanowski and T. Lukasiewicz, Appl. Phys. B. 83, 255, (2006).

[16] W. Ryba-Romanowski, M. Berkowski, B. Viana and P. Aschehoug, Appl. Phys. B. 64, 525, (1997)

[17] A. Ferrier, C. W. Thiel, B. Tumino, M. O. Ramirez, L. E. Bausá, R. L. Cone, A. Ikesue and P. Goldner, Phys. Rev. B 87, 041102, (2013).

[18] N. Kunkel, A. Ferrier, C. W. Thiel, M. O. Ramirez, L. E. Bausa, R. L. Cone, A. Ikesue and P. Goldner, APL Materials 3, 096103, (2015).

[19] M. Kokta, J. Solid State Chem. 8, 39 (1973)

[20] C. D. Brandle and R. L. Barns, J. Crystal Growth. 20, 1 (1973).

[21] W. Van Erk and J. M. Robertson, J. Crystal Growth. 59, 543-547, (1982).

[22] J. Rodriguez-Carvajal, FULLPROF.2k: Rietveld, profile matching and integrated intensity refinement of X-ray and neutron data, V 1.9c, Laboratoire Léon Brillouin, CEA, Saclay, France, (2001). https://www.ill.eu/sites/fullprof/.

[23] A. A. Kaminskii, Crystalline Laser: Physical Processes and Operating Schemes, ISBN: 0-8493-3720-8, CRC Press, 1996.

[24] R. D. Shannon and C. T. Prewitt, Acta Cryst. (1969). B25, 925.

[25] A. Nakatsuka, A. Yoshiasa and T. Yamanaka, Acta Crystallogr., Sec. B: Struc. Sci., 55, 216 (1999).

[26] M. Nikl, E. Mihokova, J. Pejchal, A. Vedda and Y. Zorenko, Phys. Stat. Sol. (b), vol. 242, R119, (2005).

[27] Y. Zorenko, V. Gorbenko, I. Konstankevych, A. Voloshinovskii, G.Stryganyuk, V. Mikhailin, V. Kolobanov and D. Spassky, J. Lumin. 114, 85 (2005).

[28] M. K. Ashurov, Y. K. Voronko, V. V. Osiko, A. A. Sobol, B. P. Starikov and M. I. Timoschechkin, Phys. Stat. Sol. (a) 42, 101 (1977).

[29] Spectral data from the website of Remote Sensing Branch of NASA Langley Research Center [DB/OL]Page laser modified: July 7, 2016. https://lasersdb.larc.nasa.gov

[30] A. I. Burshtein, Zh. Espk. Teor. Fiz. 62, 1699 (1972) [Sov. Phys. JETP 35, 457 (1972)]

[31] R. L. Ahlefeldt, M. F. Pascual-Winter, A. Louchet-Chauvet, T. Chanelière and J.-L. Le Gouët, Phys. Rev. B 92, 094305 (2015).

[32] A. M. Stoneham, Rev. Mod. Phys. 41 (1) 82, (1969).

[33] M. Koshan, K. Yang, M. Zhuravleva and C. L. Melcher, J. Crystal Growth 352, 133-136, (2012).